HEFAT2010
7th International Conference on Heat Transfer, Fluid Mechanics and Thermodynamics
19-21 July 2010
Antalya, Turkey

NUMERICAL MODELING AND EXPERIMENTAL INVESTIGATION OF HEAT TRANSFER AND FLUID FLOW DURING LASER WELDING OF AA 5083 ALUMINIUM

Lamas M.I.*, Yáñez A.J., Tobar M.J., Sánchez-Amaya J.M., Boukha Z., Botana F.J.
*Author for correspondence
Departamento de Construcciónes Navais,
Escola Politécnica Superior,
Universidade da Coruña,
Mendizábal s/n 15403, Ferrol, A Coruña,
Spain,
E-mail: isabellamas@udc.es

ABSTRACT

In this paper, a three-dimensional numerical model was developed to study laser welding in aluminium alloys. The computational fluid dynamics (CFD) was used to solve the governing equations of conservation of mass, momentum and energy, so as to obtain the morphology, velocity field and temperature field of the melted zone in steady state. As expected, the heat transfer and fluid flow inside the melt pool are dominated by heat conduction and Marangoni convection. In particular, the surface tension coefficient is negative for aluminium alloys, so thermocapillarity tends to produce weld beads with increased (width/depth) aspect ratios. The predicted dimensions of the weld pool agreed well with experimental results obtained on aluminum (Al-Mg) alloys.

INTRODUCTION

Laser welding is an important industrial activity which is used in a wide variety of process due to its low heat input, high flexibility, high weld quality and high production rate. Two welding regimes are possible depending on processing conditions: Keyhole (or deep penetration) laser welding at high power densities, typically above 10^6 W/cm^2, and Conduction (or conduction limited) laser welding bellow this limit. In the first mode, the input laser energy causes vaporization of material along the laser scan, allowing for deep penetration into the welded piece. Although mostly used, this regime can be thermodynamically unstable and lead to pore formation and microstructural defects on the welding bead. In the Conduction mode, however, due to the reduced energy input, vaporization is minimized. Though this implies a limited penetration onto the processed part, the process becomes more stable and has benefits on the quality of the welding bead.

Although several studies have reported many advantages in using laser welding, there still exists the fundamental problem that the welding reliability of aluminium alloys is lower than that of other industrial metals, such as steels, due to its higher reflectivity, higher thermal conductivity and lower viscosity. In fact, the thermal conductivity of the aluminium alloys is about one order of magnitude higher than that of steels. Thus, the thermal conductivity of low carbon steel is ~14 W/m-K, being 130 W/m-K for the aluminium alloy AA 5083. Another important point to take into account is the high reflectivity of the aluminium alloys, which can be higher than 80%, being more reflective as the aluminium alloy is purer. Thus, the high reflectivity makes the aluminium alloys absorb little fraction of the incident radiation, the high thermal conductivity provokes a rapid heat transfer, avoiding the concentration of energy in the weld pool and finally, the lower viscosity of the welding pool limits the expansion of the pool before the solidification.

In this work, conduction laser welding in the aluminium AA 5083 alloy was studied. The aluminium AA 5083 is an alloy of the 5000 series (Al-Mg) characterized by its good formability and corrosion resistance. Advances in processing technology of these types of materials, in particular fast and high quality joining techniques, are of most interest for the automotive, chemical, marine or aeronautic industries.

A computational fluid dynamic (CFD) model was developed and numerical results were compared with experimental ones performed by means of a high power (1500 W) diode laser on aluminium plates with different surface preparations and at different scanning speeds. The main

objective of the present work was to study the influence of both the processing rate and the superficial treatment.

This paper is organized as follows. Firstly, we present the model description and governing equations. Secondly, we briefly describe the numerical method. Thirdly, we discuss the experimental and numerical results and finally we present the conclusions of this work and outline the areas of future research.

NOMENCLATURE

g	[m/s^2]	Gravity acceleration
c_p	[J/kg-K]	Specific heat
k	[W/m-K]	Thermal conductivity
p	[Pa]	Pressure
T	[K]	Temperature
T_{ref}	[K]	Reference temperature for Boussinesq approximation
t	[s]	Time
V	[m/s]	Velocity
V_{laser}	[m]	Laser velocity
a	[ ]	Absorption coefficient
A	[ ]	Smoothed liquid fraction
B	[ ]	A very small number introduced to avoid division by zero
C	[ ]	A very large positive number
h	[J/kg]	Enthalpy
$S_{velocity}$	[kg/m^{2}s^2]	Momentum source due to zero velocity solid
s	[ ]	Unit tangential vector
n	[ ]	Unit normal vector

Special characters

β	[K^{-1}]	Thermal expansion coefficient
σ	[N/m-K]	Temperature coefficient of surface tension
μ	[Pa-s]	Dynamic viscosity
ρ	[m]	Density
Φ	[W/m^2]	Heat flux
α_l	[ ]	Liquid fraction
L	[J/kg]	Latent heat of melting

Subscripts

liquid	Liquid
solid	Solid
ref	Reference

MATHEMATICAL MODEL

Model Description

In the 1980's, the first significant progress were developed in the solution of the equations of conservation of mass, momentum and energy in fusion welding. Relevant works are [1-3], which studied the melting process using stationary heat sources.

In practice, the heat source moves with a certain constant velocity. Thus, when viewed in a fixed coordinate system, the welding problem is unsteady. Several investigations of fluid flow and heat transfer in welding using governing equations formulated in this coordinate system were reported [4-7]. The disadvantage of an unsteady simulation is that accurate results require a very refined mesh, which makes the computation time be very large.

Another approach is to work in a coordinate system which moves with the heat source. In such a case, for a constant welding velocity and a long metal sample, the problem becomes steady in a short time after the start of welding. Under such conditions, the heat source and the molten metal under the heat source are fixed in space and the material enters and leaves the computational domain at the welding velocity [8-12]. For this case, the computation time is much smaller than for unsteady simulations.

In this study, a coordinate system attached to the heat source was used to study a three-dimensional aluminium sample. The geometry is shown in **Figure 1.** As the laser moves away from the workpiece, a fraction of the incident energy is absorbed and leads to rapid heating, melting and vigorous circulation of the molten material in the weld pool. Convective driving forces of melting liquid in the molten pool come from two sources: one is the surface tension or Marangoni force (due to the surface tension gradient along free interface), and the other, much less important, is the buoyancy force (due to the density difference in the liquid metal pool). These forces were considered for the calculation of weld pool convection.

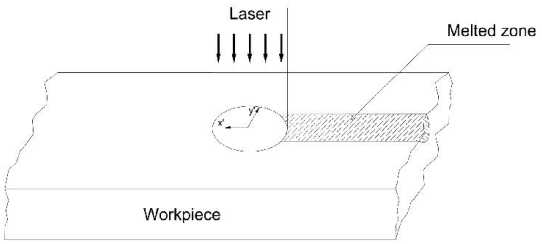

Figure 1. Schematic representation of the model.

In order to transform the problem into a simpler one, the following assumptions were made:

- Steady state in the coordinate system moving with the laser beam.
- Laminar flow.
- Boussinesq approximation (because the variation of density with temperature is small but no negligible).
- Symmetry.
- Negligible deformation on the top surface of the melt pool.
- Conduction laser welding (not Keyhole laser welding).
- Constant properties (except the surface tension).

Governing equations

As the governing equations were formulated in a reference frame attached to the moving heat source, they were modified by subdividing the net velocity into the convective and the welding velocity components as follows:

$$\vec{V} = \vec{V} + \vec{V}_{laser} \tag{1}$$

Using equation (1), the steady state versions of the modified governing equations were derived in [10] and [12]. The final form is given as follows:

- *Continuity conservation equation:*

$$\nabla \cdot \vec{V} = 0 \tag{2}$$

- *Momentum conservation equation:*

$$\nabla \cdot (\rho \vec{V} \vec{V}) = -\nabla p + \nabla \cdot (\mu \nabla \vec{V}) - \rho \vec{g} \beta (T - T_{ref}) - \nabla \cdot (\rho \vec{V}_{laser} \vec{V}) + S_{velocity} \tag{3}$$

where $S_{velocity}$, given by equation (4), represents the source term that modifies the momentum equation in the mushy zone [10], [12], [13].

$$S_{velocity} = A \cdot \vec{V} \tag{4}$$

where:

$$A = -C \left(\frac{1 - \alpha_l^2}{\alpha_l^3 + B} \right) \tag{5}$$

α_l is the smoothed liquid fraction, given by equation (6). It indicates the fraction of the cell volume that is in liquid form.

$$\alpha_l = \frac{T - T_{solid}}{T_{liquid} - T_{solid}} \tag{6}$$

For the cases studied, a temperature difference of 40 K was assumed between the liquid and solid, and a temperature of 848 K was assumed as the melting point, so T_{solid} = 828 K and T_{liquid} = 868 K.

- *Energy conservation equation:*

Instead of tracking the liquid-solid front explicitly, the liquid-solid mushy zone was treated as a porous zone. The mushy zone is a region in which the liquid fraction lies between 0 and 1. An enthalpy-porosity technique [13], [14] was used for modeling the melting process. In this technique, the enthalpy of the material is computed as the sum of the sensible enthalpy, h, and the latent heat, L:

$$h = h_{ref} + \int_{T_{ref}}^{T} c_p dT + \alpha_l L \tag{7}$$

Finally, the modified energy equation is given by:

$$\nabla \cdot (\rho \vec{V} h) = k \nabla^2 T - \nabla \cdot (\rho \vec{V}_{laser} h) \tag{8}$$

Boundary conditions

The boundary conditions are shown in **Table 1** and **Figure 2**. At the bottom and lateral walls, the velocity is set to zero (no slip) and the temperature is set to ambient temperature. At the symmetry, the velocity gradient and the temperature gradient are set to zero. Finally, at the top wall, the Marangoni effect and the laser heat flux, Φ, act.

Table 1. Boundary conditions for energy and momentum equations.

Zone	Boundary condition energy eq.	Boundary condition momentum eq.
Top wall	$-k \frac{\partial T}{\partial z} = \phi$	$\tau = \mu \frac{\partial \vec{V}}{\partial n} = \left\lvert \frac{\partial \sigma}{\partial T} \right\rvert \frac{\partial T}{\partial s}$ (only for the melted zone)
Bottom wall	$T = T_{ambient}$	$\vec{V} = 0$
Lateral walls	$T = T_{ambient}$	$\vec{V} = 0$
Symmetry wall	$\frac{\partial T}{\partial y} = 0$	$\frac{\partial \vec{V}}{\partial y} = 0$

Numerical procedure

The governing equations were solved using the commercial software Ansys Fluent 6.3, which is based on the control volume method.

A fixed mesh was used and a single set of continuity, momentum and energy equation was shared by both phases liquid and solid. As can be seen in **Figure 2**, the domain was discretized using an hexahedral grid, with finer size mesh (0.05 mm) near the heat source and coarser (1 mm) farther the heat source. The size of the samples was approximately 70x20x5 mm.

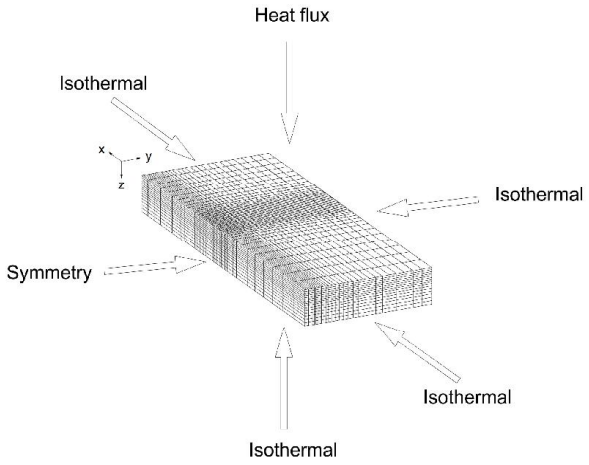

Figure 2. Mesh and boundary conditions.

The velocity-pressure coupling in the momentum equations was handled using the SIMPLE (Semi-Implicit Method for Pressure-Linked Equations) algorithm and the momentum and energy equations were discretized by the second order upwind scheme.

RESULTS AND DISCUSSIONS

Description of the experimental tests

The experimental tests were developed elsewhere [17] by a high power diode laser of Rofin-Sinar with a maximum power of 2800 W. All the laser treatments were performed in continuous mode at 1500 W. The heat flux corresponding to the laser intensity mapping is depicted in **Figure 3**, as measured at laser focus. As can be seen in **Figure 3,** the laser spot size at focus is 1.772 x 2.272 mm.

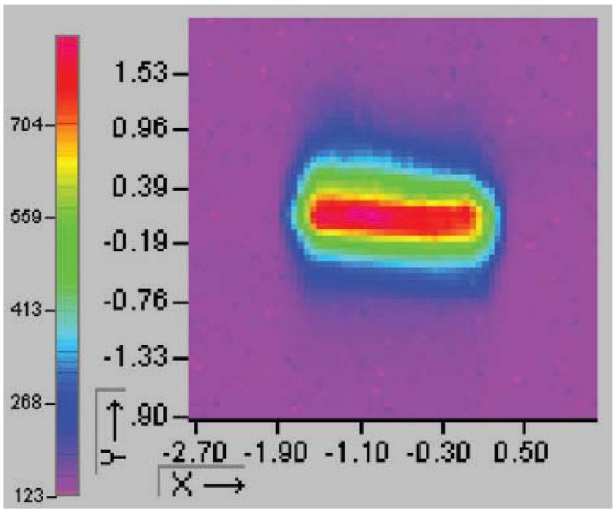

Figure 3. Laser focus spot shape.

The laser heat flux is transferred to the body by thermal radiation. When the laser radiation is incident on the surface, a portion is absorbed in the material and the remainder is reflected from the surface. The magnitude which represents the fraction of the total radiation absorbed by the body is called absorptivity or absorption coefficient. Nowadays, the determination of the absorptivity is not completely understood because it depends of a lot of aspects such as laser wavelength, surface characteristics, temperature, etc. In the present work, the variation of absorption with temperature and other factors was neglected and only the influence of the surface characteristics was considered. The superficial treatments which were applied on the aluminium plates before being irradiated with laser were the following:

- *Treatment I.* The samples were grounded to a superficial roughness of 2.2 µm and covered by a black marker layer.
- *Treatment II.* The samples were grounded and subjected to a chemical cleaning treatment. The superficial roughness was 2.2 µm. Finally, as in treatment I, the samples were covered by a black marker layer.
- *Treatment III.* The samples were blasted, increasing their roughness up to 50 µm.

For the cases studied, the laser was moved at constant velocity. In order to evaluate the influence of the processing rate on the characteristics of the generated weld beads, two welding velocities were considered: v_1 = 25 mm/s and v_2 = 50 mm/s.

To sum up, two laser processing rates and three superficial treatments were employed. The codes employed in this paper to identify each condition are included in **Table 2**.

Table 2. Codes to identify superficial treatments and laser velocities.

Sample code	Superficial treatment	Laser velocity
TIv_1	TI: grounded + black marker layer	v_1 = 25 mm/s
TIv_2	TI: grounded + black marker layer	v_2 = 50 mm/s
$TIIv_1$	TII: grounded + chemical cleaning treatment + black marker layer	v_1 = 25 mm/s
$TIIv_2$	TII: grounded + chemical cleaning treatment + black marker layer	v_2 = 50 mm/s
$TIIIv_1$	TIII: blasted	v_1 = 25 mm/s
$TIIIv_2$	TIII: blasted	v_2 = 50 mm/s

The properties of the aluminium AA 5083 used in the computations are presented in **Table 3.**

Table 3. Properties of AA 5083 aluminium.

Density (kg/m^3)	2700
Viscosity (kg/m-s)	0.0005
Thermal conductivity (W/m-K)	130
Latent heat of melting (J/kg)	388000
Specific heat (J/kg-K)	903
Coefficient of thermal expansion (K^{-1})	24·10^{-6}
Temperature coefficient of surface tension (N/m-K)	-0.000125
Melting point (K)	848

Numerical and experimental results

1- Temperature field

The steady temperature field is shown in **Figure 4.** The typical elongated pool shape due to the laser movement can be appreciated. As expected, the temperature gradients are greater in front of the moving heat source than behind the heat source.

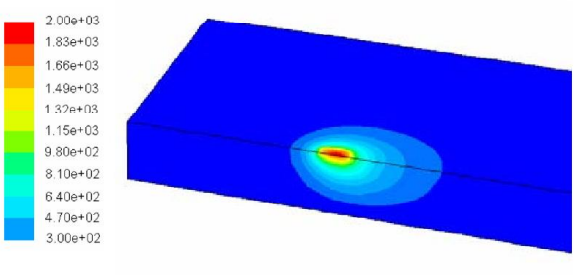

Figure 4. Steady temperature field for $TIIv_1$ conditions.

The values of the maximum temperatures obtained numerically varied from 1630 K (for $TIIIv_2$) to 1960 K (for $TIIv_1$), so the boiling point, which for the AA 5083 aluminium is approximately 2800 K, was not reached in any case. This is consistent with the fact of modeling Conduction laser welding instead of Keyhole laser welding.

2- Velocity field

The velocity field in the molten pool is shown in **Figure 5**. For clarity, only the section of the computational domain just below the heat source is shown in the figure.

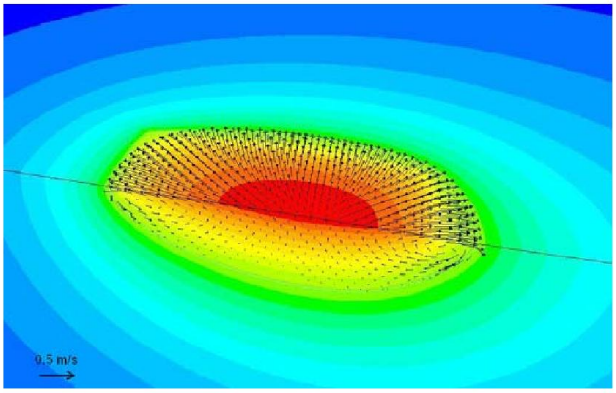

Figure 5. Steady velocity field for TIv_1 conditions.

The values of the maximum velocities obtained numerically were 10^{-1} order for all the cases studied.

From **Figure 5**, it can be seen how the liquid metal moves from the center, where the temperature is high, toward the periphery, where the metal has a relatively low temperature. This is expected for a metal with a very low concentration of surface active elements, which results in a negative temperature coefficient of surface tension [15], [16]. In the present paper, all the calculations assumed a constant negative temperature coefficient of surface tension.

3- Determination of the absorption coefficient

The absorption coefficient for each treatment is not known a priory. The procedure used to determine it is as follows: For the treatment I, an absorption coefficient was estimated for v_1 velocity (TIv_1) from an adjustment of the depth and then it was verified if the supposed value was consistent for v_2 velocity (TIv_1). The procedure for the treatment II and the treatment III was the same. The values of the radiation absorption coefficient resulted 0.42, 0.43 and 0.35 for the treatments I, II and III respectively. The treatment III leads to lower values of absorption coefficient than the treatments I and II. This means that black marker layers are more effective in increasing laser absorption than blasting procedures to increase roughness.

4- Depth and width of the weld pool

A metallographic image of the weld bead cross-section of the TIv_1 sample is included in **Figure 6**. In this image, the width and depth of the weld bead were marked with arrows. In a previous work [17], both parameters were measured in AA 5083 samples subjected to the six treatments described before (TIv_1, TIv_2, $TIIv_1$, $TIIv_2$, $TIIIv_1$ and $TIIIv_2$).

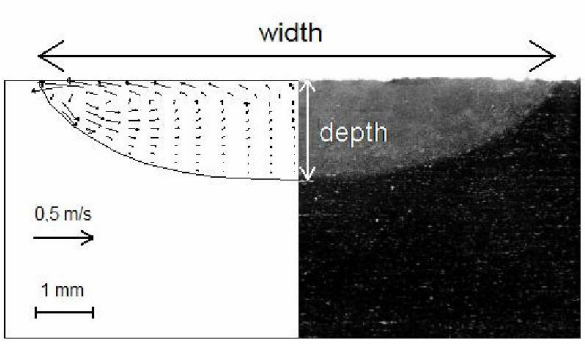

Figure 6. Calculated weld pool cross sections and metallographic image for TIv_1.

The numerical and experimental values of the weld bead depth and width are included in **Figures 7 and Figure 8** respectively. A reasonable agreement can be observed between experimental and calculated results.

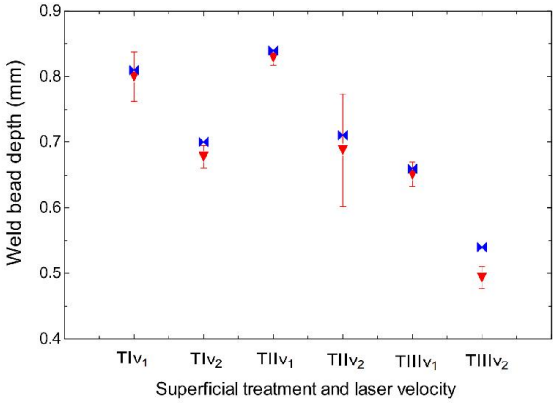

Figure 7. Mean and standard deviation values of experimental weld beads depths and comparison with numerical results.

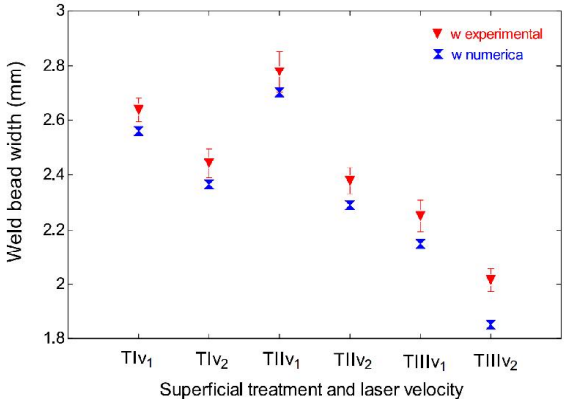

Figure 8. Mean and standard deviation values of experimental weld beads widths and comparison with numerical results.

The differences between the weld bead dimensions are due to the different total amount of laser energy absorbed per unit surface along the laser scan. Therefore, at the same laser power and scanning speed, the TI and TII samples show a bigger penetration than TIII samples due to the higher laser absorption coefficient. Respect to the effect of the scanning speed, it should be noted that at the same laser power, the energy input per unit surface diminishes with the increase in the laser scan velocity. Therefore, for all the treatments, weld beads are larger for lower scanning speeds. In particular, when the processing rate is decreased from v_2 to v_1, the penetration increases by 18% for TI, 20% for TII and 32% for TIII.

CONCLUSIONS

In the present paper, a computational analysis of the heat transfer and fluid flow during welding with a moving heat source was developed. The governing equations were formulated in the reference frame attached to the moving heat source. The equations were modified to treat the physical velocity of the liquid metal relative to the sample as the primary unknown velocity. This modification results in physically meaningful source terms that contain the effect of the moving source term in the governing equations.

The numerical results were compared with experimental ones, obtained by a high power diode laser working at a continuous power of 1500 W. The influence on both the processing rate and the superficial treatments was analyzed and it was confirmed that the model correctly reproduces the aspect ratio of the weld bead for all the conditions studied.

Based on these results, it is concluded that the developed model may serve as an optimizing tool for laser (conduction) welding. The analysis of the process parameters in terms of the input power, laser spot size and scanning speed may yield the best combination in terms of required penetration and welding quality.

REFERENCES

[1] Kou, S., Sun, D.K., 1985, Fluid flow and weld penetration in stationary arc welds, *Metallurgical and Materials Transactions A*, vol. 16, pp. 203-213, 1985.

[2] Zacharia, T., David, S.A., Vitek, J.M., DebRoy, T., 1989, Weld Pool Development during GTA and Laser Beam Welding of Type 304 Stainless Steel, Part 1: Theoretical Analysis, *Welding Journal* 68, 12, pp 499-509.

[3] Paul, A., DebRoy, T., 1988, Free surface flow and heat transfer in conduction mode laser welding, *Metallurgical and Material Transactions B,* vol. 19, number 6, pp. 851-858.

[4] Zacharia, T., David, S.A., Vitek, J.M., DebRoy, T., 1990, Modeling of interfacial phenomena in welding, *Metallurgical and Material Transactions B,* vol. 21, number 3, pp. 600-603.

[5] Chan, C., Mazumder, J., Chen, M.M., 1984, A two-dimensional transient model for convection in laser melted pool, *Metallurgical and Materials Transactions A*, vol. 15, pp. 2175-2184.

[6] Yang, L.X., Peng, X.F., Wang, B.X., 2001, Numerical modeling and experimental investigation on the characteristics of molten pool during laser processing, *International Journal of Heat and Mass Transfer*, vol. 44, pp. 4465-4473.

[7] Mahrle, A., Beyer, E., Transient behaviour of laser induced axisymmetric melt pools, *18th Meeting on Mathematical Modelling of Materials Processing with Lasers*, 2005.

[8] Kou, S., Wang, Y.H., 1986, Three-dimensional convection in laser melted pools, *Metallurgical and Materials Transactions A*, vol. 17, number 12, pp. 2265-2270.

[9] Prakash, C., Sammonds, M., Singhal, A.K., 1987, A fixed grid numerical methodology for phase change problems involving a heat source, *International Journal of Heat and Mass Transfer*, vol. 30, number 12, pp. 2690-2694.

[10] Mundra, K., DebRoy, T., Kelkar, K.M., 1996, Numerical prediction of fluid flow and heat transfer in welding with a moving heat source, *Numerical Heat Transfer A*, vol. 29, pp. 115-129.

[11] Li, J.F., Li, L., Stott, F.H., 2004, A three-dimensional numerical model for a convection-diffusion phase change process during laser melting of ceramic materials, *International Journal of Heat and Mass Transfer*, vol. 47, pp. 5523-5539.

[12] Lamas Galdo, M.I., Tobar Vidal, M.J., Yáñez Casal, A.J., 2009, Estudio numérico de la influencia de la termocapilaridad en soldadura láser por conducción, *VI Jornadas Nacionales de Ingeniería Termodinámica, JNIT 2009.*

[13] FLUENT 6.3 Documentation, 2006, FLUENT Inc.

[14] Voller, V.R., Prakash, C., 1987, A fixed grid numerical modeling methodology for convection-diffusion mushy region phase-change problems, *International Journal of Heat and Mass Transfer,* vol. 30, pp. 1790-1719.

[15] Pierce, S.W., Burgardt, P., Olson, D.L., 1999, Thermocapillary and arc phenomena in stainless steel welding, *Welding Research Supplement*, pp. 45-52.

[16] Mills, K., Keene, B.J., Brooks, R.F., Shirali, A., 1998, Marangoni effects in welding, *Phil. Trans. R. Soc. Lond. A,* vol. 356, pp. 911-925.

[17] Sánchez-Amaya, J.M., Delgado, T., De Damborenea, J.J., López, V., Botana, F.J., 2009, Laser welding of AA 5083 samples by high power diode laser, *Science and Technology of Welding and Joining,* vol. 14, number 1, pp. 78-86.